Lawrence Livermore National Laboratory

LLNL-JRNL-2003969

Ab-initio prediction of rapid kinetics of Fe impurities in δ-Pu

B Sadigh, P Soderlind, K Kweon

July 2025

Disclaimer

This work performed under the auspices of the U.S. Department of Energy by Lawrence Livermore National Laboratory under Contract DE-AC52-07NA27344.

Ab-initio prediction of rapid kinetics of Fe impurities in δ-Pu

Kyoung E. Kweon,[1, a)] Per Söderlind,[1] and Babak Sadigh[1, b)]
Lawrence Livermore National Laboratory, Livermore, CA, 94550

(Dated: 1 July 2025)

We study the formation energies of iron impurities in δ-Pu within spin-orbital-polarized density functional theory (SOP-DFT). The thermodynamic solubility limit of iron in δ-Pu is calculated, indicating low miscibility. We show that surprisingly, Fe impurities at equilibrium are almost equally likely to occupy octahedral interstitial sites or substitutional sites, with slight preference for the former. In contrast, we find the energy of the tetrahedral interstitial Fe to be nearly 1 eV higher than the octahedral one. We explore the energy landscape for Fe impurity hopping diffusion and conclude that Fe impurities in δ-Pu are divided into two populations: (i) immobile substitutional Fe impurities, and (ii) highly mobile interstitial Fe impurities. The latter, (ii), migrate between octahedral interstitial sites with an energy barrier of around 0.2 eV. The energy barrier for exchange between the two populations is calculated to exceed 0.7 eV. Finally, we discuss the role of magnetic order on the impurity energetics.

I. INTRODUCTION

The material properties of plutonium metal and its alloys are critical to nuclear fuel and other applications, particularly at elevated temperatures where these applications operate[1–4]. Understanding plutonium-iron alloys is important because of the ubiquitous use of steel containers in nuclear reactor applications as well as for nuclear waste storage[5–8]. The Pu-Fe phase diagram is well-known[9,10]. Iron dissolves poorly in plutonium and impurities are known to have low miscibility in a plutonium metal. At Fe concentrations larger than the solubility limit the $\mathrm{Pu_6Fe}$ compound is formed[11,12]. A crucial factor determining the kinetics of second-phase formation is the rate of impurity diffusion in the dilute limit. In this article, we examine the mechanisms governing the diffusion of Fe impurities in the Pu host lattice and demonstrate that *ab initio* calculations predict a high degree of mobility for iron in this system.

Plutonium is perhaps the most complex elemental metal with a polymorphic phase diagram consisting of six different solid phases at ambient pressure[13,14]. Considering the low melting temperature of plutonium, all these phases exist within a narrow temperature range thus suggesting a very competitive phase landscape. In spite of that, an important feature of the solid-solid phase transitions is that they involve large volume changes. As a result, the specific volume of the ground state low-symmetry α-phase is known to be 20% smaller than the high-symmetry (face-centered cubic, fcc) δ-phase. Conventional non-magnetic Kohn-Sham density-functional theory (KS-DFT) using the traditional exchange-correlation schemes, such as e.g., LDA or GGA, is unable to reproduce the observed density changes between the different solid phases or even realistic energies[15]. However, allowing for spin polarization and inclusion of relativistic corrections via addition of spin-orbit coupling (SO) can account for about 75% of the volume difference between the α and the δ-Pu phase[16]. In addition, incorporation of second Hund's rule coupling via orbital polarization functionals (OP) can account for the remaining 25% of the density change observed between the two Pu phases[17,18]. In the following, we refer to this combination of spin-polarized KS-DFT, SO and OP, as spin-orbital-polarized DFT (SOP-DFT).

The SOP-DFT has been applied to the calculations of energies and volumes of the different solid phases of pure Pu[17,18], as well as a number of Pu compounds[19–22]. A salient feature of these calculations is the formation of large spin and orbital moments on the Pu atoms, which couple strongly to the neighboring sites and order antiferromagnetically. It should be noted that the spin and orbital moments at the Pu sites are of nearly equal magnitude but oriented in opposite directions, resulting in a small net moment on each plutonium atom. This is simply a straightforward consequence of Hund's rules for a less than half filled $5f$ band. Nevertheless, the emerging consensus is that the electronic structure of Pu metal is understood in terms of dynamic magnetism, i.e., fluctuating spin and orbital moments[23,24]. This conclusion is not inconsistent with SOP-DFT as this theory is also expected to predict a multitude of nearly degenerate low-lying spin/orbital configurations. In practice, for SOP-DFT calculations of materials properties, the static approximation is currently the only computationally feasible approach. However, the effect of magnetic fluctuations can to an extent be analyzed by studying the variability of calculated properties with respect to spin and orbital ordering.

Recently, SOP-DFT has been used in investigations of the structures and energetics of lattice defects in δ-Pu[16]. It was found that vacancies and self-interstitials behave radically differently in different Pu phases, and these behaviors are at odds with the corresponding properties of the transition metals. For instance, in contrast to almost all close-packed metals, equilibrium self-interstitial population is predicted to be much higher than vacancies in δ-Pu. In this article, we investigate the energy landscape of Fe impurities in the δ-Pu lattice within SOP-DFT. We calculate the solubility of Fe in this phase, and explore several mechanisms for impurity diffusion. We will show that at equilibrium, iron, the impurity population, is divided into two nearly equisized populations, one consisting of highly mobile interstitial species, and another immobile substitutional species. The energy barrier for exchange of parti-

---

a)Electronic mail: kweon1@llnl.gov
b)Electronic mail: sadigh1@llnl.gov

cles between the two groups is calculated to be relatively large and exceeding 0.8 eV.

It should be noted that lattice defect and impurity calculations require relatively large supercells. As a result, SOP-DFT calculations in Pu become computationally demanding and prone to slow convergence to charge self-consistency. This challenge arises from the spin and orbital degrees of freedom existing within a multivalley energy landscape with shallow energy barriers, leading to sluggish collective relaxation toward the ground state. In this work, we explore the energetics of Fe impurities in δ-Pu within three low-energy spin configurations. We found that spin configurations that are metastable for the perfect δ-Pu lattice become unstable in the presence of an Fe impurity, and transition to lower energy spin configurations. This is observed even for a low-energy spin configuration such as high-symmetry 3Q configuration, commonly employed in calculations for the perfect δ-Pu lattice[25–28]. Consequently, care must be taken to estimate the energy released from bulk spin relaxations and exclude it from the calculated impurity energies. Ultimately, we find that the energy landscape of the Fe impurity remains consistent across the different spin arrangements.

II. METHODOLOGY

In this paper, we investigate the potential energy landscape of Fe impurities in δ-Pu within SOP-DFT, as implemented in the Vienna Ab initio Simulation Package (VASP)[29]. The SOP-DFT total energy is based on the standard SP-DFT total energy functional with the wavefunctions represented in a projector augmented wave (PAW) basis[30] employing a planewave cutoff of 600 eV. The electron exchange and correlation energy is calculated using the generalized-gradient approximation (GGA) in the PBE[31] parameterization. In addition, relativistic corrections and second Hund's rule coupling are incorporated via SO and OP terms. The SO and OP treatments are non-standard and need further explanation. First, regarding the implementation of SO coupling, in order to mitigate the error caused by the absence of the $p_{1/2}$-orbital in the scalar relativistic PAW basis used in VASP, we explained in a previous paper that for actinides it suffices to omit the spin-orbit coupling to the p-angular momentum channel[32]. Second, regarding the implementation of OP, we follow the fully variational development within the PAW basis described in previous papers[16,32], where the OP functional is the sum (over ions) of the squares of the total f-orbital moments within each atomic sphere projected onto the direction of the orientation of the local spin moment. In the present work, we introduce a small modification to this scheme in order to be more faithful to the original formulation proposed by Brooks and coworkers[33,34]. As a result, the OP functional is implemented as the sum (over spin channels and ions) of the squares of the spin-resolved f-orbital moments within each atomic sphere. The detailed description of the fully variational implementation of this strategy within the PAW scheme will be described elsewhere.

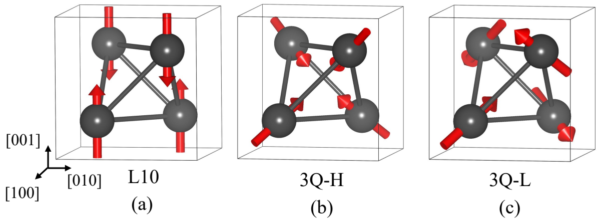

FIG. 1. Conventional unit cell of δ-Pu with different spin configurations (a) L10, (b) 3Q-H, and (c) 3Q-L. The red arrow represents the spin moment direction vector (of unit length) per each atom. The gray ball denotes Pu atom.

TABLE I. Bulk properties of δ-Pu with different spin configurations with experimental values[39,40]

Property	L10	3Q-H	3Q-L	Exp.
Eq. volume (Å^3/Pu)	24.9	25.0	24.9	25.2
Rel. energy (meV/Pu)	0.0	6.0	-2.0	–
Bulk modulus (GPa)	38.6	37.5	38.1	30-35

Within Brook's original scheme, the OP functional is parameterized via the Racah parameter, which for f-orbitals is denoted by E^3 and can be expressed as a linear combination of the F_2, F_4, and F_6 Slater integrals of the site-projected wavefunctions for each spin channel, calculated self-consistently. In the fully variational scheme developed in Ref. [32], this parameter is treated as a constant, identical for all spin channels. In the present work, we use the value 0.056 eV for the OP strength parameter of Pu that is close (but somewhat smaller) than the relevant average of Racah parameters calculated self-consistently.[35] For Fe, only SO treatment is included. The orbital polarization has an effect on the 3d states, but is very small in this context and can safely be ignored.[36] The aim of this paper is to study the thermodynamics and kinetics of Fe impurities in δ-Pu. Fe impurities and lattice defects are studied in 32 and 108-atom supercells. Structural relaxations, including changes in cell shape and volume, induced by lattice defects and impurities are performed until the atomic forces derived within the PAW scheme are smaller than 0.01 eV/Å. The Brillouin-zone is sampled by a Monkhorst-Pack grid equivalent to the $12 \times 12 \times 12$ mesh for the 4-atom fcc primitive cell, $4 \times 4 \times 4$ mesh for the 32-atom supercell, and $3 \times 3 \times 3$ mesh for the 108-atom supercell, respectively. We employ the solid-state nudged elastic band (ss-NEB) method[37] to calculate the migration energy barrier of Fe impurity. The climbing image algorithm[38] with three intermediates is employed to accurately determine the energy at the saddle point of the migration pathway.

III. RESULTS AND DISCUSSION

A. Perfect δ-Pu lattice

SOP-DFT predicts that large spin and orbital moments form on the Pu atoms in the δ-Pu lattice. The arrangement of these moments is predominantly driven by exchange coupling between neighboring Pu atoms leading to antiferromagnetic order, which can be quantified at any site i as the sum of the dot products of its spin moment direction vector (of unit length) with those of the nearest neighbors, denoted by γ_i. On the fcc lattice, it can be shown that maximal antiferromagnetic order corresponds to $\gamma_i = -4$. There are a multitude of non-collinear spin arrangements that satisfy this condition. Figure 1 shows three such spin configurations, which have been employed in the present work to assess the sensitivity of the calculated impurity energetics on the choice of spin arrangement.

Two of the spin configurations in Fig. 1, i.e. L10 in (a) and 3Q-H in (b), have been used in past studies of δ-Pu. It should be noted that the 3Q-H notation for the spin configuration in Fig. 1(b), is non-standard. The conventional notation in the literature is simply 3Q. However, for reasons that will soon become clear, we intentionally refer to this configuration as 3Q-H in this paper.

The L10 spin configuration, consisting of ferromagnetic fcc-(001) layers, with spin orientation of each layer being opposite to its two adjacent layers leading to $\gamma_i = -4$, has been used extensively in the past to study the materials properties of the δ-Pu lattice[16,41–44]. It does produce reasonable results for materials properties of δ-Pu, but it exhibits a lower symmetry (tetragonal) than the cubic symmetry of the fcc lattice, resulting in a slight tetragonal symmetry breaking at ambient pressure. To mitigate this problem, Rudin used the non-collinear 3Q-H spin configuration, see Fig. 1(b), to study the properties of δ-Pu lattice in Ref. [25]. This spin configuration preserves the cubic symmetry of the fcc lattice, and has been adopted in several subsequent works on the thermodynamic properties of defects and H impurities in δ-Pu.[25–28]

The 3Q-H configuration is not the only spin arrangement that preserves the cubic symmetry of the fcc lattice. As shown in Fig. 1(c), there exists another distinct spin configuration, which we refer to as 3Q-L, that also exhibits cubic symmetry. Both 3Q-H and 3Q-L configurations are arranged so that the angle between any pair of nearest-neighbor (NN) spins equals $109.47°$, leading to $\gamma_i = -4$. The distinction between the two spin configurations lies in the orientation of the spin moments relative to the vectors connecting NN pairs. In the 3Q-L configuration, the vector connecting each NN pair is orthogonal to one of the spin moments, while in the 3Q-H configuration, this condition is not satisfied for any NN pair. To our knowledge, the 3Q-L configuration has not previously been considered, in the context of δ-Pu electronic structure. In the following, we conduct a comparative study of the L10, 3Q-H, and 3Q-L spin configurations, for bulk properties of the δ-Pu phase, and for energetics of the Fe impurities in the δ-Pu crystal.

Table I presents the relative energies of the three spin configurations at their respective equilibrium volumes. Among these, the 3Q-L represents the lowest energy state and the 3Q-H the highest. Table I also demonstrates that the variations of equilibrium volumes and bulk moduli across the three spin configurations are small, and in good agreement with experiments.

TABLE II. Zero-pressure mixing enthalpies (ΔH_m in eV) and relaxation volumes (ΔV_r per atomic volume of the δ-Pu) of Fe impurities in δ-Pu calculated using 2×2×2 supercells (32 atoms) and 3×3×3 supercells (108 atoms) with the L10 initial Pu lattice spin configuration. For Fe_{Pu} and $\text{Fe}_{i,oct}$, the mixing enthalpies calculated using a constant-volume approach (without cell volume relaxation) are provided in parentheses. Fe interstitial configurations at the octahedral ($\text{Fe}_{i,oct}$) and at the tetrahedral sites ($\text{Fe}_{i,tet}$) are illustrated above the table, with the corresponding polyhedra represented as shaded.

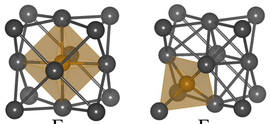

$\text{Fe}_{i,\text{oct}}$ $\text{Fe}_{i,\text{tet}}$

	2x2x2 supercell		3x3x3 supercell	
	ΔH_m (eV)	ΔV_r (/atomic vol.)	ΔH_m (eV)	ΔV_r (/atomic vol.)
Fe_{Pu}	0.90 (0.96)	-0.68	0.90 (0.93)	-0.81
$\text{Fe}_{\text{i,oct}}$	0.84 (0.91)	0.88	0.88 (0.90)	0.81
$\text{Fe}_{\text{i,tet}}$	1.84 (1.90)	0.80	1.87 (1.90)	0.65

B. Fe impurity thermodynamics

Table II presents the mixing enthalpies and relaxation volumes of Fe impurities at zero pressure in substitutional, octahedral interstitial, and tetrahedral interstitial positions in the L10 spin configuration. The mixing enthalpies ΔH_m are calculated via the expression

$$\Delta H_m = H_{sc} - N_{\text{Pu}} H_{\delta\text{-Pu}} - H_{\text{bcc-Fe}}, \tag{1}$$

where H_{sc} is the zero-pressure enthalpy of a periodic supercell containing N_{Pu} Pu atoms occupying an fcc lattice along with a single Fe impurity atom obtained by fully optimizing cell shape and volume as well as atomic positions, and $H_{\delta\text{-Pu}}$ and $H_{\text{bcc-Fe}}$ are the per-atom zero-pressure enthalpies of the δ-Pu and the bcc-Fe crystals respectively. Table II shows the results for two supercell sizes, providing a measure for the strength of impurity image interactions. The dependence of the results on supercell size and spin configuration will be discussed in greater detail later in this section. A notable finding is that the Fe impurity at equilibrium most likely resides on octahedral interstitial sites. This is quite unexpected but is a consequence of ΔH_m for substitutional Fe being slightly higher than octahedral interstitial Fe. In contrast, the tetrahedral interstitial sites are strongly disfavored. Nevertheless, the calculated ΔH_m of 0.84 eV for the octahedral interstitial site in the L10 spin configuration is indicative of the low miscibility of Fe in δ-Pu. We find a finite magnetic moment of 2.54 μ_B for Fe at the Fe_{Pu} which aligns with the original lattice Pu spin

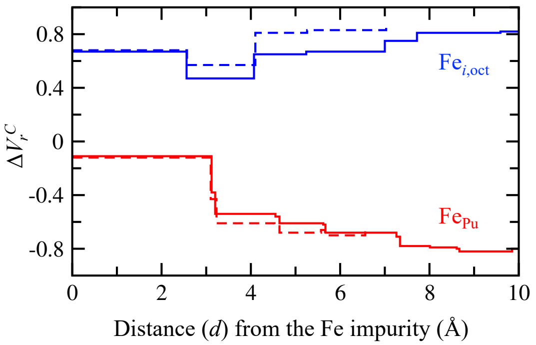

FIG. 2. Cumulative formation volume as a function of distance from the Fe impurity. Two different supercell sizes, 2×2×2 (dashed line) and 3×3×3 (solid line), with the L10 initial spin configuration. Fe_{Pu} and $\text{Fe}_{i,oct}$ are represented by red and blue lines, respectively (Color online). Each species is annotated with a label for clarity in black and white print. The cumulative formation volumes are given in units of per-atom equilibrium volume of the respective perfect δ-Pu.

orientation, whereas Fe exhibits no magnetic moment when located at interstitial positions. Because Fe itself is magnetic, this is a counterintuitive result that will be analyzed in the future. Here it suffices to say that the nonmagnetic state of Fe also exists in crystal structure more closely packed than bcc.

The relaxation volume ΔV_r, quantifies the magnitude of the strain field induced by a defect or an impurity atom in the host lattice. ΔV_r in Tab. II are calculated according to the following expression

$$\Delta V_r = \frac{(V_{sc} - N^0_{\text{Pu}}\Omega_{\text{Pu}})}{\Omega_{\text{Pu}}}, \tag{2}$$

where N^0_{Pu} is the number of Pu atoms in a perfect lattice supercell prior to introduction of a defect or impurity, V_{sc} is the volume of the supercell containing the defect or impurity, and Ω_{Pu} is the per-atom volume of the δ-Pu phase. The relaxation volumes in Tab. II are given in fractions of Ω_{Pu}. It is noteworthy that the Fe impurity in the substitutional site causes a significant volume contraction, comparable in magnitude to that induced by the vacancy in δ-Pu, as reported in Ref. [16]. Similarly, the volume relaxations associated with interstitial Fe impurities closely resemble those of the self-interstitials in δ-Pu.[16]

The dependence of the zero-pressure mixing enthalpies and relaxation volumes on the supercell size are shown in Tab. II. No qualitative change in the results are observed with change of system size. In order to achieve a deeper understanding of the volume relaxations around the impurity atom, we analyze the distribution of relaxations by Voronoi decomposition of the impurity supercells. Figure 2 illustrates the accumulated contribution to the relaxation volume as a function of distance d, originating from the spherical region within a radius d from the Fe impurity atom, defined as

$$\Delta V_r^C(d) = \frac{\omega_{\text{Fe}}}{\Omega_{\text{Pu}}} + (N_{\text{Pu}} - N^0_{\text{Pu}}) + \sum_{i=1}^{N_{\text{Pu}}} \left(\frac{\omega_i}{\Omega_{\text{Pu}}} - 1 \right) H(d - d_i), \tag{3}$$

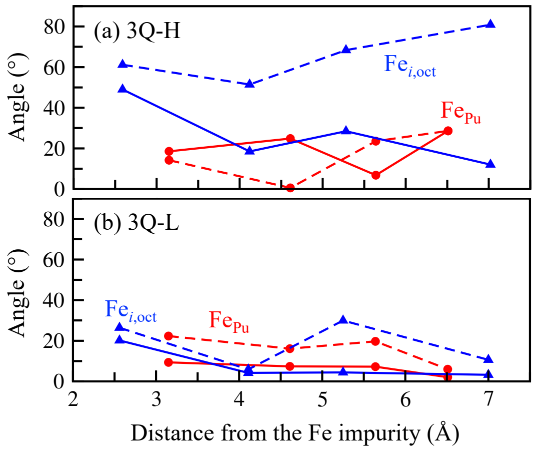

FIG. 3. Angles between the initial and the final relaxed spin orientations of the Pu atoms as a function of their distances to the Fe impurity atom. The results of calculations in 2×2×2 supercells for Fe_{Pu} are shown in red lines with circle symbols and $\text{Fe}_{i,oct}$ in blue lines with triangle symbols (Color online). Dashed lines represent changes in the spin orientations of the Pu atoms in impurity supercells initiated from (a) 3Q-H and (b) 3Q-L configurations. Solid lines represent changes in spin orientations of the Pu atoms in supercells with the Fe impurity removed, but initiated from the final relaxed spin configurations that were obtained through impurity calculations originally initiated in (a) 3Q-H and (b) 3Q-L, respectively.

where ω_i and d_i are the Voronoi volume of the ith Pu atom and its distance from the Fe impurity respectively, ω_{Fe} is the Voronoi volume of the Fe impurity atom, and $H(x)$ is the Heavyside function with $H(x) = 0$ for $x < 0$, and otherwise $H(x) = 1$. For an impurity embedded in a host material that can be characterized by isotropic linear elasticity, the cumulative relaxation volume $\Delta V_r^C(d)$ provides a rigorous measure for the extent of the non-linear core region around an impurity, where non-linear interatomic interactions are essential. This is because in an isotropic continuum elastic medium, the dilatational strain field due to a misfit inclusion decays as square of the distance away from the inclusion, and thus the volume relaxation integrated over a spherical shell around the inclusion is independent of its radius. As a result, the radial extent d_c of the non-linear core region can be defined as the distance, beyond which $\Delta V_r^C(d)$ approaches a nearly constant value. Examining Fig. 2, the non-linear core region is observed to extend to several neighbor shells. The non-elastic interactions originate from the unconventional electronic bonding in δ-Pu driven by spin and orbital moment formation, and their coupling to lattice relaxations.

It is worth noting that the mixing enthalpies of Fe_{Pu} and $\text{Fe}_{i,oct}$ in 2x2x2 supercells, calculated using a constant-volume approach (without cell volume relaxations), are 0.96 eV and 0.91 eV, respectively. However, when defect-induced lattice strains are fully relaxed through volume and cell shape optimization, these values decrease to 0.90 eV and 0.84 eV, respectively. In the larger 3x3x3 supercells, the mixing enthalpies calculated using the constant-pressure and constant-volume methods approach each other.

TABLE III. Zero-pressure mixing enthalpies (ΔH_m in eV) of $\mathrm{Fe_{Pu}}$ and $\mathrm{Fe}_{i,oct}$, calculated using 2×2×2 supercells initialized with the L10, 3Q-H, and 3Q-L spin configurations. For 3Q-H and 3Q-L, ΔH_m are provided relative to the perfect lattice energies calculated both in the initial spin configuration, labeled ”Initial”, and final relaxed spin configuration, labeled ”Final”. Details are discussed in the text.

	L10	3Q-H		3Q-L	
		Initial	Final	Initial	Final
$\mathrm{Fe_{Pu}}$	0.90	0.88	0.96	0.94	0.96
$\mathrm{Fe_{i,oct}}$	0.84	0.48	0.82	0.78	0.80

Finally, we discuss the effect of spin configuration on impurity energetics. This is an important topic and needs to be studied in some detail. As discussed in the Introduction, the electronic structure in Pu is believed to be characterized by dynamic magnetism. However, static magnetism is currently the only computationally practical approach for our computationally demanding supercell calculations. In the following, we analyze the effect of magnetic configuration fluctuations on mixing enthalpies of Fe impurities, by exploring how sensitive the calculated values are to the choice of spin arrangement.

Table III presents calculated values of ΔH_m for the 3Q-H and 3Q-L spin configurations. Before delving into these results, it is important to address a complicating factor: for any atomic configuration, only a subset of spin/orbital configurations, i.e., those that are metastable, and correspond to local minima of the SOP-DFT energy landscape, can be accessed by ground-state calculations. It is reasonable to expect that the number of metastable spin configurations can be significantly different for atomic configurations with different symmetries. Thus, starting from a spin configuration that is metastable in perfect δ-Pu, the introduction of an Fe impurity can destabilize this configuration, making it energetically favorable to transition to a lower-energy (magnetic-electronic) configuration in the bulk. This is a magnetic transition that shall not occur in reality but a consequenc of the metastable nature of the initial magnetic state.

This stability of a spin configuration with respect to a local perturbation, e.g., addition of an Fe impurity, can be assessed rigorously by monitoring the change in spin moment directions of the Pu atoms as a function of their distance from the perturbation. The hallmark of stable spin configurations is the diminishing effect of perturbations on the spin state of Pu atoms as the distance from the perturbation increases. In other words, the defect should not affect the electronic-magnetic structure far from its location. Figure 3 depicts the changes in spin orientations of the Pu host atoms in response to addition of an Fe impurity, plotted as a function of the distance from the impurity, for the 3Q-H and 3Q-L spin configurations. The L10 configuration remains stable upon inclusion of an Fe impurity, exhibiting negligible changes in spin orientations (not shown). In contrast, the 3Q-H and 3Q-L configurations (depicted as dashed lines in Figure 3) exhibit changes in their spin orientations, with the 3Q-H configuration showing a substantially larger variation. Non-vanishing changes in spin orientations observed far from the impurity suggest bulk spin instability and transformation to a lower-energy spin configuration. This leads to artificially low ΔH_m in finite supercells, as shown in Tab. III for Fe impurities initiated with the 3Q-H spin order. In the dilute limit, ΔH_m is expected to diverge due to the bulk spin instability. This renders the 3Q-H spin order not suitable for Fe impurity calculations.

A strategy to obtain convergent ΔH_m in the dilute limit from calculations initialized with an unstable spin configuration is to calculate the perfect lattice energy $H_{\delta\text{-Pu}}$ using the final spin configuration obtained after the relaxation of the impurity supercell. The aim of this procedure is to match the spin configurations of the perfect lattice and impurity supercells in order to make Eqs. 1 and 2 internally consistent. In Tab. III, ΔH_m are reported under the labels 3Q-H or 3Q-L following two procedures: (i) (labeled ”Initial”) the same spin configuration (3Q-H or 3Q-L) is used to initialize the perfect lattice and the impurity supercell calculations, and (ii) (labeled ”Final”) the impurity supercell is initialized in the 3Q-H or 3Q-L spin configuration, and subsequently the perfect lattice is initialized in a spin configuration that is matched to the final spin configuration obtained from relaxation of the impurity supercell. As expected, the ΔH_m values calculated via procedure (ii) are always higher than those calculated via procedure (i), since the energy of the perfect lattice is lower in the former case. Specially noteworthy is the case of $\mathrm{Fe}_{i,oct}$ initialized in the 3Q-H spin configuration. Table III demonstrates that procedure (ii) significantly corrects the artificially low ΔH_m values resulting from the instability of the 3Q-H spin configuration induced by the Fe impurity.

Finally, it can be concluded from Tab. III that overall, the calculated impurity properties, are consistent across spin configurations. The largest difference is found in the ΔH_m of $\mathrm{Fe_{Pu}}$, which is almost 7% higher in the 3Q-L arrangement compared to the L10.

C. Fe impurity kinetics

In this section, we discuss the most important impurity migration mechanisms and their associated energy barriers. As discussed in the previous section, at equilibrium, the population of Fe impurities is dominated by two species: substitutional and octahedral interstitial. For these species, the two most important migration pathways depicted in Figure 4(a) are : (I) along one of the face diagonals: $(1,1,0),(1,0,1),(0,1,1)$, leading to migration of an Fe impurity from one octahedral interstitial site to a neighboring one, and (II) along one of the cube axes: $(100),(010),(001)$, leading to transformation of an Fe impurity from an octahedral interstitial site to becoming $\mathrm{Fe_{Pu}}$ with a neighboring $\mathrm{Pu}_{i,oct}$. Conversely, for a $\mathrm{Fe_{Pu}}$ to migrate, it must capture a Pu self-interstitial, and subsequently migrate together along a cube axis, and as a result, the Fe impurity transitions to an octahedral interstitial position, and the Pu self-interstitial occupies the vacant substitutional site left behind. Hence, the defect

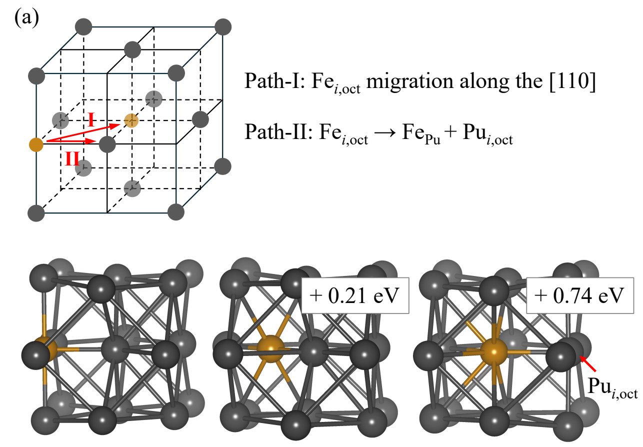

(b) $\mathrm{Fe}_{i,\mathrm{oct}}$ (c) TS in Path-I (d) $\mathrm{Fe}_{\mathrm{Pu}} + \mathrm{Pu}_{i,\mathrm{oct}}$

FIG. 4. (a) Schematic of two $\mathrm{Fe}_{i,oct}$ migration pathways in fcc lattices. Path-I represents Fe interstitial migration along the [110] direction, while Path-II represents Fe interstitialcy mechanism along the [100], which displaces a lattice Pu, forming $\mathrm{Fe}_{\mathrm{Pu}}$ and $\mathrm{Pu}_{i,oct}$. Atomic configurations are shown for (b) $\mathrm{Fe}_{i,oct}$, (c) transition state (TS) along Path-I, and (d) $\mathrm{Fe}_{\mathrm{Pu}}$ + $\mathrm{Pu}_{i,oct}$ in Path-II. The relative energies of the configurations in (c) and (d) with respect to $\mathrm{Fe}_{i,oct}$ in (b) are also indicated.

complex composed of an Fe substitutional impurity and an octahedral Pu self-interstitial can be considered an intermediate state (approximating a transition state) for the transformation between the two dominant Fe impurity species: substitutional and octahedral interstitial.

Figure 4(b)-(d) illustrates the geometries of the octahedral interstitial, and the transition states for the two migration pathways. The energy barriers for the two transition pathways are calculated using 32-atom supercells within the SOP-DFT framework. For pathway I, the ss-NEB method was employed to examine the diffusion of $\mathrm{Fe}_{i,oct}$ to adjacent interstitial sites. The calculated energy barrier for pathway I is 0.21 eV, which increases slightly to 0.25 eV when the volume of the intermediates is fixed during the transition. The minimal energy difference between these two energies implies minor structural changes during the transition. These low energy barriers suggest fast interstitial diffusion. For pathway II, an explicit NEB calculation was not performed due to the significantly higher energy difference of 0.74 eV between the $\mathrm{Fe}_{\mathrm{Pu}}$ + $\mathrm{Pu}_{i,oct}$ complex and $\mathrm{Fe}_{i,oct}$. This 0.74 eV energy difference represents a lower bound for the energy barrier along pathway II.

The picture that emerges from the calculation presented in this work is that the equilibrium population of Fe impurities in the dilute limit is divided between immobile substitutional impurities, and highly mobile octahedral interstitial impurities. The rate of exchange between the two populations is determined by a transition mechanism with a relatively high energy barrier exceeding 0.78 eV.

IV. CONCLUSION

In this paper, we have studied the kinetics of Fe impurities in δ-Pu from first principles, using the SOP-DFT framework. A new fully variational implementation of Brook's OP scheme has been employed, leading to accurate calculations of bulk thermodynamic properties of δ-Pu, with large spin and orbital moments forming on the Pu atoms. Supercell calculations of impurity mixing enthalpies has revealed that at equilibrium the population Fe impurities are divided between octahedral interstitial and substitutional character, with the former being energetically favored by a small amount. We discuss in some detail the complications that can arise, originating from the dynamic magnetism in δ-Pu, for calculations of thermodynamic properties of defects and disorder in this system. We conclude by mapping out the energy landscape for Fe impurity diffusion, and find a low migration barrier (≈ 0.2 eV) for octahedral interstitial Fe diffusion, compared to a much larger barrier (≈ 0.7 eV) for an immobile substitutional Fe impurity to migrate to an octahedral interstitial position.

ACKNOWLEDGMENTS

The work at the Lawrence Livermore National Laboratory was performed under the auspices of the U.S. Department of Energy (DOE) under Contract No. DE-AC52-07NA27344. We acknowledge the Livermore Computing (LC) facility for providing high-performance computing resources. We thank Tien Roehling, Scott B. Donald, Lorin Benedict, and Nathan Barton for helpful discussions and for project support.

AUTHOR DECLARATIONS

Conflict of interest

The authors have no conflicts to disclose

DATA AVAILABILITY

The data that support the findings of this study are available from the corresponding author upon reasonable request.

[1] J. Kittel, J. Ayer, W. Beck, M. Brodsky, D. O'Boyle, S. Zegler, F. Ellinger, W. Miner, F. Schonfeld, and R. Nelson, "Plutonium and plutonium alloys as nuclear fuel materials," Nuclear Engineering and Design **15**, 373–440 (1971).

[2] S. S. Hecker, "Plutonium and its alloys," Los Alamos Science **26**, 290 (2000).

[3] S. S. Hecker and M. Stan, "Properties of plutonium and its alloys for use as fast reactor fuels," Journal of Nuclear Materials **383**, 112–118 (2008), advances in Nuclear Materials: Processing, Performance and Phenomena.

[4] P. G. Allen, P. A. Turchi, and G. F. Gallegos, "Thermodynamics and structure of plutonium alloys," Tech. Rep. (Lawrence Livermore National Lab. (LLNL), Livermore, CA (United States), 2004).

[5] J. Haschke and J. Martz, "Plutonium storage," Encyclopedia of Environmental Analysis and Remediation **6**, 3740 (1998).

[6] J. M. Haschke and J. L. Stakebake, "Handling, storage, and disposition of plutonium and uranium," in *The chemistry of the actinide and transactinide elements* (Springer, 2006) pp. 3199–3272.

[7] P. Barthelemy and R. Boucher, "Study of u-pu-fe alloys (masurca critical experiment)," Tech. Rep. (CEA Fontenay-aux-Roses, 1965).

[8] E. E. Moore, P. E. Turchi, A. Landa, P. Söderlind, B. Oudot, J. L. Belof, S. A. Stout, and A. Perron, "Development of a calphad thermodynamic database for pu-u-fe-ga alloys," Applied Sciences **9**, 5040 (2019).

[9] P. Mardon, H. Haines, J. Pearce, and M. Waldron, "The plutonium-iron system," J. Inst. Metals **86** (1957).

[10] O. K. von Goldbeck, "Fe—pu iron—plutonium," in *IRON—Binary Phase Diagrams* (Springer Berlin Heidelberg, Berlin, Heidelberg, 1982) pp. 94–96.

[11] K. Moore, M. Wall, and A. Schwartz, "Experimental verification of the existence and structure of ζ pu6fe in a pu–ga alloy," Journal of nuclear materials **306**, 213–217 (2002).

[12] J. D. Coe, W. W. Anderson, and P. H. Tobash, "The melt enthalpy of pu6fe," Applied Sciences **11**, 10800 (2021).

[13] R. Albers, "An expanding view of plutonium," Nature **410**, 759–761 (2001).

[14] A. M. Boring and J. L. Smith, "Plutonium condensed-matter physics," Los Alamos Science **26**, 90 (2000).

[15] P. Söderlind, J. Wills, B. Johansson, and O. Eriksson, "Structural properties of plutonium from first-principles theory," Physical Review B **55** (1997).

[16] B. Sadigh, P. Söderlind, N. Goldman, and M. P. Surh, "Ab initio calculations for void swelling bias in α-and δ-plutonium," Physical Review Materials **6**, 045005 (2022).

[17] P. Söderlind and B. Sadigh, "Density-functional calculations of α, β, γ, δ, δ, and plutonium," Physical review letters **92**, 185702 (2004).

[18] P. Söderlind, "Quantifying the importance of orbital over spin correlations in δ-pu within density-functional theory," Physical Review B—Condensed Matter and Materials Physics **77**, 085101 (2008).

[19] A. Landa and P. Söderlind, "First-principles calculations of stability of δ-pu–am alloys," Journal of alloys and compounds **376**, 62–67 (2004).

[20] P. Söderlind, A. Landa, A. Perron, E. E. Moore, and C. Wu, "Thermodynamics of plutonium monocarbide from anharmonic and relativistic theory," Applied Sciences **10**, 6524 (2020).

[21] P. Söderlind, "Density-functional electronic structure of pucoga 5," Physical Review B—Condensed Matter and Materials Physics **70**, 094515 (2004).

[22] P. Söderlind, A. Landa, J. Klepeis, Y. Suzuki, and A. Migliori, "Elastic properties of pu metal and pu-ga alloys," Physical Review B—Condensed Matter and Materials Physics **81**, 224110 (2010).

[23] M. Janoschek, G. Lander, J. M. Lawrence, E. D. Bauer, J. C. Lashley, M. Lumsden, D. L. Abernathy, and J. D. Thompson, "Relevance of kondo physics for the temperature dependence of the bulk modulus in plutonium," Proceedings of the National Academy of Sciences **114**, E268–E268 (2017).

[24] B. Amadon, "First-principles dft+ dmft calculations of structural properties of actinides: Role of hund's exchange, spin-orbit coupling, and crystal structure," Physical Review B **94**, 115148 (2016).

[25] S. P. Rudin, "Symmetry-correct bonding in density functional theory calculations for delta phase pu," Journal of nuclear materials **570**, 153954 (2022).

[26] P. Söderlind, A. Landa, L. Yang, B. Sadigh, and S. P. Rudin, "Lattice dynamics and thermodynamics for δ-plutonium from density functional theory," Physical Review B **108**, 104112 (2023).

[27] F. Bottin, R. Béjaud, B. Amadon, L. Baguet, M. Torrent, A. Castellano, and J. Bouchet, "Huge anharmonic effects in delta plutonium," Physical Review B **109**, L060304 (2024).

[28] A. Muñoz, I. Matanovic, B. Gifford, S. Rudin, T. Holland, and T. Jones, "Electronic structure and thermodynamic approaches to the prospect of super abundant vacancies in δ-pu," Physical Chemistry Chemical Physics **26**, 12661–12671 (2024).

[29] G. Kresse and J. Furthmüller, "Efficient iterative schemes for ab initio total-energy calculations using a plane-wave basis set," Physical review B **54**, 11169 (1996).

[30] G. Kresse and D. Joubert, "From ultrasoft pseudopotentials to the projector augmented-wave method," Physical review b **59**, 1758 (1999).

[31] J. P. Perdew, K. Burke, and M. Ernzerhof, "Generalized gradient approximation made simple," Physical review letters **77**, 3865 (1996).

[32] B. Sadigh, A. Kutepov, A. Landa, and P. Söderlind, "Assessing relativistic effects and electron correlation in the actinide metals th to pu," Applied Sciences **9**, 5020 (2019).

[33] M. Brooks and P. Kelly, "Large orbital-moment contribution to 5 f band magnetism," Physical review letters **51**, 1708 (1983).

[34] O. Eriksson, M. Brooks, and B. Johansson, "Orbital polarization in narrow-band systems: Application to volume collapses in light lanthanides," Physical Review B **41**, 7311 (1990).

[35] P. Söderlind, "Ambient pressure phase diagram of plutonium: A unified theory for α-pu and δ-pu," Europhysics Letters **55**, 525 (2001).

[36] P. Söderlind, O. Eriksson, B. Johansson, R. Albers, and A. Boring, "Spin and orbital magnetism in fe-co and co-ni alloys," Physical Review B **45**, 12911 (1992).

[37] D. Sheppard, P. Xiao, W. Chemelewski, D. D. Johnson, and G. Henkelman, "A generalized solid-state nudged elastic band method," The Journal of chemical physics **136** (2012).

[38] G. Henkelman, B. P. Uberuaga, and H. Jónsson, "A climbing image nudged elastic band method for finding saddle points and minimum energy paths," The Journal of chemical physics **113**, 9901–9904 (2000).

[39] O. J. Wick *et al.*, "Plutonium handbook: a guide to the technology," (No Title) (1967).

[40] H. Blank and R. Lindner, *Plutonium 1975 and Other Actinides: Proceedings of the Conference in Baden Baden, September 10-13, 1975* (North-Holland, 1976).

[41] S. C. Hernandez, F. J. Freibert, R. G. Hoagland, B. P. Uberuaga, and J. M. Wills, "Spin density stabilization of local distortions induced by a monovacancy in δ-pu," Physical Review Materials **2**, 085005 (2018).

[42] S. K. Barman, S. C. Hernandez, and R. Atta-Fynn, "A first-principles study on ga stabilized δ-pu phase stability based on structural and electronic properties," Computational Materials Science **231**, 112533 (2024).

[43] S. C. Hernandez, F. J. Freibert, B. P. Uberuaga, and J. M. Wills, "Role of electronic and magnetic interactions in defect formation and anomalous diffusion in δ-pu," Journal of nuclear materials **532**, 152027 (2020).

[44] S. C. Hernandez, F. J. Freibert, and J. M. Wills, "Density functional theory study of defects in unalloyed δ-pu," Scripta Materialia **134**, 57–60 (2017).